Article

China Coastal Front from Himawari-8 AHI SST Data. Part 1: East China Sea

Igor M Belkin *, Shang-Shang Lou, Wen-Bin Yin

Posted Date: 9 January 2023

doi: 10.20944/preprints202301.0147.v1

Keywords: China Coastal Front; Zhejiang-Fujian Front; Zhe-Min Front; Himawari-8; Advanced Himawari Imager; East China Sea; Taiwan Strait; Sea surface temperature

Article

China Coastal Front from *Himawari-8* AHI SST Data. Part 1: East China Sea

Igor M. Belkin *, Shang-Shang Lou and Wen-Bin Yin

College of Marine Science and Technology, Zhejiang Ocean University, Zhoushan, China
* Correspondence: igagsa@uri.edu

Abstract: High-resolution (2 km) high-frequency (hourly) SST data from 2015-2020 provided by the Advanced Himawari Imager (AHI) onboard the Japanese *Himawari-8* geostationary satellite positioned over 140.7°E were used to study spatial and temporal variability of the China Coastal Front (CCF) in the East China Sea. The hourly SST data were processed with the Belkin and O'Reilly (2009) algorithm to generate long-term mean monthly maps of SST gradient magnitude (GM) and frontal frequency (FM) using a GM threshold of 0.1°C/km. Horizontal structure of SST field in the vicinity of the CCF was investigated from cross-frontal distributions of SST along 8 parallels from 31°N to 24°N. The high resolution (2 km) monthly distributions of SST along these 8 parallels were used to determine inshore and offshore boundaries of the CCF and calculate the CCF strength defined as the total cross-frontal SST step dSST=Offshore SST – Inshore SST. The CCF emerges in November, fully develops in December and peaks in strength in January-February. The front's fragmentation and shrinking/weakening begins in February and March, respectively. In winter (December-February), the front's strength dSST exceeds 5°C offshore the Zhejiang-Fujian coast and could be as high as 7.5°C when nearshore waters cool down to 7°C. In winter, the front's strength decreases downstream from 31°N to 24°N. The CCF changes its physical nature as the seasons progress. In winter, the CCF is a water mass front between cold and fresh water coming from the north and warm and salty water coming from the south. In summer, the CCF becomes a coastal upwelling front maintained largely by southerly winds. In winter, the CCF's cross-frontal structure in the SST field is ramp-shaped, with SST increasing monotonously in the offshore direction. In summer, the CCF's cross-frontal structure in the SST field is V-shaped or U-shaped, featuring a minimum SST formed by cold upwelled water at some distance from the shore. Thus, the summer SST structure effectively consists of two fronts, a nearshore and offshore, with a minimum SST in-between. Across the inshore/offshore front, the SST decreases/increases in the offshore direction. The local bathymetry, especially the relatively steep shelf slope between 20-m and 50-m isobath, steers the front, which does not meander in winter offshore the Zhejiang-Fujian coast. As the cold season progresses, the front's axis gradually shifts into deeper waters, from ~20 m to ~50 m.

Keywords: China Coastal Front; Zhejiang-Fujian Front; Zhe-Min Front; Himawari-8; advanced Himawari imager; East China Sea; Taiwan Strait; sea surface temperature

1. Introduction

The China Coastal Current (CCC) is the most robust large-scale circulation feature in the East China Seas. The spatial stability of the CCC stems from the strong topographic control exerted by the coast and shallow bathymetry of the shelf. Even though the CCC reverses its direction twice a year following the seasonal monsoons, the CCC location over the inner shelf remains remarkably stable. Because of its proximity to the coast heavily populated by several hundred million people that live and work in the most economically advanced provinces of China, the CCC and associated ocean front (China Coastal Front, CCF) are of tremendous importance to various maritime activities such as fisheries, aquaculture, transportation, tourism, recreation, human health, weather/climate forecasts etc. Despite the paramount importance of the CCC and CCF, dedicated studies of the CCC and CCF

Preprints (www.preprints.org) | NOT PEER-REVIEWED | Posted: 9 January 2023 doi:10.20944/preprints202301.0147.v1

are relatively rare. Most studies on the East China Sea and southern Yellow Sea focused on offshore circulation and fronts over middle and outer shelf (50-200 m depth), reviewed recently by Liu ZQ et al. (2021). In situ studies of inshore oceanography of this region are logistically challenging due to the shallow bathymetry of the inner shelf, where the rugged coastline and myriads of small islands complicate ship surveys. Satellite observations are free from the above logistical constrains. Since the advent of satellite oceanography, the CCF was studied from remote sensing data, first and foremost from sea surface temperature (SST) data. **Table 1** sums up a provisional inventory of remote sensing studies of the CCF from SST data. These studies elucidated many important aspects of the CCF discussed below and provided a solid background for the present study. In the following chronological review of previous investigations, we cite various names used by different researchers for the CCF such as the Zhejiang Front, Zhejiang-Fujian Front, Fujian-Zhejiang Front, Zhe-Min Front, Min-Zhe Front, and Mainland China Coastal Front. Within the ECS, these names are considered synonyms unless indicated otherwise.

Table 1. Satellite studies of the China Coastal Front in the East China Sea from SST data. **Regions:** ECS, East China Sea; SECS, Southern ECS; YS, Yellow Sea; SCS, South China Sea; NSCS, Northern SCS; TS, Taiwan Strait; BYECS, Bohai-Yellow-East China Seas. **Sensors and algorithms:** AHI, Advanced Himawari Imager; BOA2009, Belkin and O'Reilly (2009); CCA1992, Cayula and Cornillon (1992); CW2014, Castelao and Wang (2014); DOISST, Daily Optimum Interpolation SST; PH2010, Pi and Hu (2010); S2005, Shimada et al. (2005); GM, Gradient magnitude; NA, Not Available. *) AVHRR, MODIS, and AMSR-E data merged.

Reference	Sensor	Period	Algorithm	Region
Belkin et al. (this study)	AHI	2015-2020	BOA2009	ECS, TS: 24-32°N, 118-124°E
Cao L et al. 2021	MODIS	2002-2017	CW2014	Inshore ECS: 26-33°N, 120-124°E
Chang et al. 2006	AVHRR	1996-2005	S2005	ECS, TS: 21-29°N, 117-124°E
Chang et al. 2008	AVHRR	1996-2005	S2005	SECS: 24-29°N, 118-124°E
Chang et al. 2010	AVHRR	2001-2007	S2005	NSCS, including TS
He MX et al. 1995	AVHRR	1984-1989	NA	ECS, YS: 26-38°N, 120-129°E
He SY et al. 2016	MODIS	2000-2013	GM	ECS: 25-30.5°N, 119-124°E
Hickox et al. 2000	AVHRR	1985-1996	CCA1992	BYECS
Huang et al. 2010	TRMM	1998-2005	GM	BYECS
Lee et al. 2015	AVHRR	1996-2009	S2005	ECS, YS: 24-35°N, 118-131°E
Liu DY et al. 2018	MODIS	2003-2015	BOA2009	ECS, YS: 24.5-41°N, 119-131°E
Ning et al. 1998	AVHRR	1981-1988	NA	ECS, YS: 21°45′-41°15′N, 118-31°45′E
Pi and Hu 2010	Misc.*	2002-2008	PH2010	18-30°N, 116-128°E
Ping et al. 2016	MODIS	2000-2013	CCA1992	22-41°N, 117-132°E
Qiao et al. 2020	MODIS	2003-2018	GM	24-32°N, 119-125°E
Wang YC et al. 2013	AVHRR	2006-2009	S2005	SECS, TS: 21-28°N, 118-124°E
Wang YC et al. 2018	AVHRR	2005-2015	S2005	SECS: 24-28°N, 119-124°E
Zhao et al., 2022	DOISST	1982-2021	CCA1992	China Seas: 0-41°N, 105-130°E

The research-quality SST data provided by the Advanced Very High Resolution Radiometer (AVHRR) flown on NOAA polar-orbiting satellites and processed under the Pathfinder project (Minnett et al., 2019) became available since 1982 and were used in numerous studies. He MX et al. (1995) used AVHRR SST data from 1984-1989 to identify 8 fronts in the East China Sea and Yellow

Sea, including the Zhejiang coastal front between 26°N and 29°N, offshore of the 50-m isobath, having a width of 10-50 km and a maximum SST gradient of 0.9 °C/km (*ibid.*, Figure 1 and Table 1). The authors pointed out that this front "exists throughout the year but has different causes between winter and summer. In winter, it is an interface between the Zhejiang coastal water diluted from the Changjiang River and the warm saline water of the TWC [Taiwan Warm Current]. Its shape, off-shore distance and horizontal SST gradient are basically determined by the variability of the TWC. In summer, the enhancement of the local upwelling interacts with the permanent TWC, giving rise to a visible surface manifestation of this front." (*ibid.*, p. 276). The authors noted (*ibid.*, p. 284) that in summer a "prominent upwelling zone is located between 25-30°N. The upwelled surface water is 5°C lower than the SST of the TWC." Regarding the physical nature of the Zhejiang upwelling, they wrote (*ibid.*, p. 286): "There have been controversies over the major cause of this upwelling … One argument states that the upwelling is primarily caused by the upward climbing of the north residual of the Kuroshio and therefore is a permanent upwelling throughout the year. Another argument suggests that the upwelling is only generated by wind in summer and therefore is a seasonal upwelling." The dual nature of the CCF has been addressed by numerous scholars and is discussed below.

Ning et al. (1998) used SST data from 1981-1986 and ocean color data from 1978-1986 to describe water masses and fronts in the ECS. Their maps of long-term monthly mean SST reveal wintertime development and summertime disappearance of the Min-Zhe coastal front along the 50-m isobath. Oddly, the monthly SST maps by Ning et al. (1998) do not show the Min-Zhe front until January, unlike those in other studies that show this front as early as October. The low resolution (18 km x 18 km) of the SST data used by Ning et al. (1998) may be accountable for the above discrepancy. Indeed, according to later studies cited below, in early winter the newly formed Min-Zhe current clings to the China coast, extending SW over very shallow water depths of 20 m or even less. Therefore, it is possible that the 18-km resolution SST data used by Ning et al. (1998) did not resolve the narrow Min-Zhe current in early winter until the current widened and shifted offshore by mid-winter.

Hickox et al. (2000) processed 9-km resolution, twice-daily Pathfinder AVHRR SST data from 1985-1996 with the Cayula and Cornillon (1992) algorithm (CCA), which detects SST fronts. Hickox et al. (2000) identified 10 fronts and determined long-term mean positions of their boundaries (offshore and inshore) from frontal frequency (FF) maps. Using maps of frontal frequency based on the BOA front detection output, Hickox et al. (2000) delineated frontal *envelopes* (or frontal *corridors*) consisting of inshore and offshore boundaries of each front and calculated long-term mean monthly SST averaged along each boundary, designated as Offshore SST and Inshore SST. Long-term mean monthly cross-frontal SST ranges (steps) were calculated as DT = Offshore SST – Inshore SST. Among other fronts, Hickox et al. (2000) distinguished the CCF, termed the Zhejiang-Fujian front, and emphasized its nature as a wintertime front best developed from December through March.

In a series of papers spanning a decade, Yi Chang and collaborators used the Shimada algorithm (Shimada et al., 2005) to detect SST fronts in the northern South China Sea and East China Sea (Chang et al., 2006; Chang et al., 2008; Chang et al., 2010; Lee et al., 2015). In a study of winter fronts in the Taiwan Strait and southern ECS, Chang et al. (2006) and Chang et al. (2008) used high-resolution (0.01°) AVHRR SST data from 1996-2005 to generate long-term monthly mean maps of SST gradient magnitude (GM) that revealed four major fronts, including the Mainland China Coastal Front (MCCF) along the 50-m isobath. The SST GM increases from December through February, when three local maxima of GM become distinct at 24.0-25.0°N, 26.5-27.0°N and 27.5-28.5°N (*ibid.*, p. 2 and Figure 2). A local minimum of SST GM near 25.5-26.0°N is hypothetically ascribed to the impact of the Min River (Fujian) (Chang et al., 2008), which discharges on average 2,000 m^3/s at 26°N (https://en.wikipedia.org/wiki/Min_River_(Fujian), retrieved 2022-08-27). Using 1-km SST data from 2001-2007, Chang et al. (2010) generated detailed maps of frontal frequency FF for December through March. In December and January, the continuous MCCF extends along the Fujian and Guangdong coasts up to Hainan. However, in February and March, the MCCF south of 25°N does not continue along the Fujian coast. Instead, the MCCF veers offshore to join the Taiwan Bank Front (TBF) located along the steep southern flank of the Bank. The MCCF-TBF merger was noted earlier by Wang DX et al. (2001), Chang et al. (2006), and Chang et al. (2008). In a follow-up paper based on 1-km 1996-2009

SST data, Lee et al. (2015) published long-term mean monthly maps of SST GM (*ibid.*, Figs. 2 and 3) that reveal heretofore unreported details of the MCCF's space-time variability. Contrary to most previous studies that placed this front either along the 50-m isobath or offshore of this isobath (He MX at al., 1995), the monthly maps of GM in Lee et al. (2015) clearly portray the MCCF well *inshore of the 50-m isobath* during the entire 8-month period of the front's visibility in SST data (September through April). Moreover, when the front emerges in September off of the Zhejiang coast, it is located *inshore of the 20-m isobath*! (*ibid.*, Figure 3C). As the season progresses, the front shifts into deeper waters, where it is found over the 20-m isobath in October-December and between the 20-m and 50-m isobaths in January-March and possibly through May.

Meanwhile, Huang et al. (2010) used the all-weather capability of the Tropical Rainfall Measuring Mission (TRMM) microwave imager (TMI) to study SST fronts in the YS and ECS from the 1998-2005 swath data with a resolution of 6 to 22 km (as opposed to the standard TMI gridded data with 0.25° x 0.25° resolution that were considered too coarse for gradient calculation). Among five coastal fronts around the YS and ECS, Huang et al. (2010) identified the Zhe-Min front, which exists from December through May, peaking in February in terms of frontal gradient magnitude GM and frontal frequency FF (for GM > 0.05°C/km). The results obtained by Huang et al. (2010) are remarkably consistent with those by Hickox et al. (2000) despite different satellite sensors, observation periods, and front detection algorithms used in these studies.

Pi and Hu (2010) studied SST fronts of the ECS and NSCS by combining various satellite data (AVHRR, MODIS, and AMSR-E) from 2002-2008 and processing this data set with a novel algorithm for mathematical morphology-based edge detection in satellite imagery. Among other fronts, the Zhe-Min Coastal Front was identified that develops in winter, peaks in April, and disappears in summer. The peak time in April is different from other studies that found the peak time in February-March. The overall pattern of seasonal evolution of the Zhe-Min Front is also qualitatively different from other studies. Although the 0.05° x 0.05° resolution (roughly 5 km) can be considered adequate for such a study, the monthly maps of frontal gradient GM in Pi and Hu (2010) appear smoothed out, which might have resulted from interpolation and smoothing applied during data reprocessing (*ibid.*, p. 1009).

Wang YC et al. (2013) combined in situ data (repeat CTD sections) and satellite SST imagery to describe the China Coastal Current Front in the southern ECS and Taiwan Strait. The SST imagery from Decembers 2006-2009 reveal the fully developed cold CCC (with SST as low as 15°C) by the end of December, while CTD data from repeat quasi-zonal sections along K Line (slant line along ~26°N) document the low-salinity (down to 30 ppt) signature of the CCC. The shallowest station (K1, 26.17°N, 120.08°E) was occupied in water depth exceeding 30 m, which illustrates bathymetric constrains that prevent ship surveys in shallow waters (<30 m). Obviously, remote sensing is not constrained by navigational hazards that impede in situ sampling of near-shore waters. Satellite imagery is especially advantageous in case of the CCC because the CCC hugs the China coast, often extending over very shallow depths (<30 m) as evidenced by CTD sections and SST maps presented by Wang YC et al. (2013). In a follow-up study, Wang YC et al. (2018) used 1-km resolution AVHRR SST data from 2005-2015 to study fronts in the SECS in winter (December through March). The Mainland China Coastal Front (MSSF) persisted along the 50-m isobath, coincident with the 14-16°C/km isotherms. The frontal SST GM of 0.20-0.40°C/km was substantially higher vs. the SST GM of 0.14°C/km in 1996-2009 (Lee et al., 2015). However, any estimates of gradients are critically dependent on data resolution and details of data processing such as gridding, smoothing etc.

Lately, researchers began using MODIS SST data that became available from 2000 onward. He SY et al. (2016) used 4-km resolution MODIS data from 2000-2013 to document a previously unreported wintertime (December-January) front along the 20-m isobath offshore the Zhe (Zhejiang) and Min (Fujian) coasts, inshore of the well-known Zhe-Min Coastal Front along the 50-m isobath. The inshore front extends from 26.5-29.5°N in December and 28.0-29.5°N in January, being relatively narrow (4-16 km) compared with the offshore front (16-48 km). He SY et al. (2016) stressed the important role of local bathymetry in the frontogenesis of both fronts. In particular, the shallow (depth < 20 m) inshore portion of the shelf widens due north, from nearly 0 km at 26.5°N up to 50 km

 doi:10.20944/preprints202301.0147.v1

at 29.5°N (*ibid.*, Figure 2). In the northern part of this wedge-shape area (north of 28.5°N), the SST in January 2007 was as low as 10°C or less (*ibid.*, Figure 1a). It seems the localized inshore cooling in this shallow area may help create a thermal east-west gradient that manifests as the inshore front.

Liu DY et al. (2018) processed 4-km resolution MODIS SST data from 2003-2015 with the Belkin and O'Reilly (2009) algorithm (BOA) to map 10 fronts between 24°N and 41°N, the same fronts as in Hickox et al. (2000). The Zhejiang-Fujian Front emerges in September offshore the Zhejiang coast; the front then grows southward and strengthens through February; then it gradually shrinks, weakens, and eventually disappears from March through August. During its maximum development in winter (December-February) the front extends north up to 32°N, where its connection to the Jiangsu Front (Hickox et al., 2000) is tenuous at best.

Qiao LL et al. (2020) used MODIS SST data from 2003-2018 to map fronts in the ECS and study their relation to the distribution of suspended sediments. This study is notable for bringing in a massive amount of in situ data collected during numerous shipborne CTD surveys. The Zhe-Min Coastal Front plays an important role by trapping most sediments. The sediment trapping by the front explains a dramatic cross-front gradient of the mud layer thickness: from 40 m underneath the front to just a few meters outside it. Qiao LL et al. (2020, Figure 7) presented 16 maps of SST gradient magnitude for individual winters 2003-2018. These maps reveal strong interannual variations of the Zhe-Min Coastal Front and smaller fronts in its vicinity. In particular, the inshore front along the 20-m isobath (He SY et al., 2016) manifests exceptionally well in winter 2005. While some interannual variations may be artifacts that are accounted for by interannual variation of cloudiness, major interannual variations in SST GM maps published by Qiao LL et al. (2020, Figure 7) are likely real.

Wang YT et al. (2020) processed 4.5-km resolution MODIS SST data from 2002-2017 with a novel front detection algorithm to study fronts in the SCS, including the Taiwan Strait up to 25°N. The seasonal variability and spatial pattern of SST fronts in the NSCS and Taiwan Strait reported by Wang YT et al. (2020) appear very similar to those in Chang et al. (2006), Chang et al. (2008), Chang et al. (2010), and Lee et al. (2015).

Cao L et al. (2021) processed 4.5-km resolution MODIS SST data from 2002-2017 with the Castelao and Wang (2014) algorithm to map fronts in the western ECS. Even though the 4-km resolution of the data used is not considered "high-resolution" these days, the frontal maps in Castelao and Wang (2014) reveal the ECS fronts in unprecedented detail. The inshore front north of 26.5°N (He SY et al., 2016) is identified in long-term mean maps of frontal gradient magnitude GM and frontal probability FP (Cao L et al., 2021, Figures 2 and 3). A relatively weak but robust SW-NE front across the Hangzhou Bay stands out year-around in FP maps (*ibid.*, Figures 2a and 3) despite being barely noticeable in the GM map (*ibid.*, Figure 2b). A peculiar but stable double-front structure of the Zhe-Min front is observed between 31-33°N, where the front is split in two branches that are best defined in October-December (*ibid.*, Figure 3a).

Zhao et al. (2022) applied the Cayula-Cornillon algorithm (CCA) to detect SST fronts in the China Seas (0-41°N, 105-130°E) using the NOAA 1/4° DOISST (Daily Optimum Interpolation SST) data set. Despite the relatively poor spatial resolution of the SST data (0.25° x 0.25°), Zhao et al. (2022) were able to detect all fronts identified by Hickox et al. (2000) and Wang DX et al. (2001) and provided monthly maps of GM based on the longest SST record to date (1982-2021).

The above studies elucidated the main features of space-time variability of the CCF. However, in most studies to date, the CCF was just a single element of a complicated frontal pattern of numerous fronts (e.g., Park and Chu, 2006; Chen, 2009; Zhao et al., 2022). After the seminal study by Hickox et al. (2000) that included a rudimentary climatology of the CCF alongside other fronts, there were no attempts to produce a comprehensive satellite data-based climatology of the CCF. In the present paper, we set out to fill this gap. In particular, save for the rudimentary climatology by Hickox et al. (2000), the cross-frontal range of SST and its seasonal and along-stream variations have not been studied. Instead, researchers focused on SST gradients. Meanwhile, it's the cross-frontal SST range (or step) that plays a crucial role in marine ecology (Belkin, 2021). The importance of this parameter is amplified by the ongoing climate change. Other aspects of the CCF that remain elusive are its

interannual variability, especially with regard to river discharge and wind forcing, and the CCF association with regional bathymetry and geomorphology.

Another objective of this study is the evaluation of data provided by the AHI flown aboard the Himawari-8 geostationary satellite, specifically the evaluation of the AHI/Himawari potential for satellite studies of ocean fronts in the China Seas. Most Earth-observing satellites are placed into sun-synchronous orbits that allow a nearly complete global coverage in a relatively short time (1-2 days), with each location observed twice a day. Geostationary satellites, in principle, allow extremely frequent observations of the same locations, with sampling frequency being only constrained by the sensor's parameters (scanning speed) and not constrained by the satellite orbit. Therefore, geostationary satellites are uniquely suited for observations of high-frequency phenomena in the ocean, including high-frequency variability of currents and fronts.

The rest of this paper is structured as follows:

1. Section 2 describes AHI/*Himawari-8* data and methods of data processing, including front detection and mapping.
2. Section 3 presents results of data processing, particularly a collection of maps and graphs that document the spatial and temporal variability of the CCF.
3. Section 4 is dedicated to a careful comparison with previous results; it also includes a brief discussion of most salient (or controversial) issues.
4. Section 5 sums up our main results and draws conclusions.

2. Data and Methods

The Japanese geostationary meteorological satellites *Himawari 8/9* (*himawari* means *sunflower* in Japanese) represent a major advancement in remote sensing of our planet (Bessho et al., 2016). Both satellites carry the Advanced Himawari Imager (AHI) that has 16 spectral bands, including 3 visible light bands (#1-3), 3 near-infrared bands (#4-6) and 10 infrared bands (#7-16). The AHI's spatial resolution is 2 km for bands #5-16; 1 km for bands #1, 2, and 4; and 500 m for band #3. The AHI provides a full disk imagery every 10 mins. Cloud-free SST composites of the full disk are available every 4 days. Owing to their location at 140.7°E and coverage range of 80°E-160°W, 60°N-60°S, these satellites are well suited for satellite studies of the China Seas. Thanks to the AHI characteristics, its data are widely used for studies of various oceanic processes, including fronts and their high-frequency variability (e.g., Hu ZF et al., 2022). The Himawari-8 satellite has been launched by the Japan Meteorological Agency (JMA) on 7 October 2014 and became operational on 7 July 2015. In this study, L3 level SST data with a temporal resolution of 1 hour and a spatial resolution of 2 km from July 2015 to December 2020 that cover our study area (24-32°N, 118-124°E) were downloaded from the P-Tree system website operated by the Japan Aerospace Exploration Agency, JAXA (https://www.eorc.jaxa.jp/ptree/). The hourly data are generated by the JAXA from the original 10-minute data. The AHI data set benefits from a radically improved cloud-masking algorithm, which takes advantage of high-resolution (500 m) visual imagery that resolves individual cumulus clouds (Bessho et al., 2016). Combined with a novel cloud-tracking algorithm and high frequency of full disk scanning (every 10 min.), this enables the production of cloud-free imagery every 4 days, which is unprecedented.

To map SST fronts associated with the CCC, we used the BOA algorithm (Belkin and O'Reilly, 2009) that generates maps of gradient magnitude (GM) and gradient direction (GD). The BOA does not generate frontal maps. Instead, a BOA user can set a GM threshold T, so that every pixel with GM>T is considered a frontal pixel. A map showing GM at frontal pixels (where GM>T) is considered a frontal map. The selection of T is inherently arbitrary. Therefore, we ran experiments with several different values of T before we have selected a particular value of T (0.1°C/km), which deemed most suitable for frontal maps. The overall frontal pattern in the study area appears quite robust and not overly sensitive to the actual choice of T.

Preprints (www.preprints.org) | NOT PEER-REVIEWED | Posted: 9 January 2023 doi:10.20944/preprints202301.0147.v1

Once frontal maps are generated, a statistical study of fronts is commenced. Following the statistical approach pioneered by Cayula and Cornillon (1992), pixel-based maps of frontal frequency FF are generated. For each pixel (array element with indices i,j), pixel-based frontal frequency FF(i,j)=N(i,j)/N(cloud-free), where N(i,j) is the total number of times the given pixel was frontal (that is GM(i,j)>FG) while N(cloud-free) is the total number of times the given pixel was cloud-free. Thus, a pair of maps of a given area – a map of GM and a map of FF – provides a complete high-resolution (pixel-based) characterization of fronts within the mapping area with two radically different and complementary metrics: gradient magnitude GM, which is a metric of front's *sharpness* (or *intensity*) and frontal frequency FF, which is a metric of front's *stability* (or *robustness*). Neither metric, however, reflects another important aspect of every front, which is front's *strength* defined as the total cross-frontal *range* (or cross-frontal *step* or *change*) of the oceanic variable in question.

In satellite oceanography, cross-frontal ranges were systematically estimated in a pioneering study by Hickox et al. (2000), who investigated seasonal variability of ten SST fronts in the East China, Yellow, and Bohai Seas. Using monthly maps of frontal frequency FF, Hickox et al. (2000) delineated offshore and inshore boundaries of the 10 fronts and calculated long-term mean monthly SST along each boundary. Thus, for each front, a pair of long-term monthly mean SST (designated as Offshore SST and Inshore SST) characterizes the cross-frontal SST range during the given month, which is calculated as a difference between these two values: SST Range = Offshore SST – Inshore SST. Of 10 fronts studied by Hickox et al. (2000), eight fronts are rather short; in such cases along-front averaging is justified. However, two other fronts (Kuroshio and CCF) are rather long; in such cases cross-frontal SST ranges are expected to change along-stream. In this study we explored the along-stream variability of monthly SST ranges across the CCF and produced a complete space-time SST climatology of the CCF.

The 10-minute and hourly SST data provided by AHI allow high-frequency phenomena (e.g., rapid development of frontal meanders and formation of frontal eddies and rings) to be investigated. The below sample of three hourly datasets (**Figure 1**) illustrates the potential of hourly data. The CCF, Kuroshio and other offshore fronts in-between (located over depths exceeding 30 m) are reproduced in each dataset, appearing fairly identical in terms of location, shape, and gradients. Conversely, numerous inshore shallow fronts between the coast and CCF (located over depths of less than 30 m) vary at the hourly scale by changing their location, shape, and gradient. Such rapidly varying shallow fronts can be studied from high-frequency data generated by AHI at *Himawari-8/9*.

The main temporal scale addressed in this study is seasonal. The CCC and associated CCF are known to develop during the winter monsoon and degenerate during the summer monsoon. Monthly data adequately resolve the seasonal monsoon-driven variability of the current and front. Our data processing started with hourly SST data that were processed with the BOA to generate maps of frontal gradient magnitude GM that were used to generate maps of frontal frequency FF for individual weeks, months, and years, and for long-term mean months (2015-2020) and years (2016-2020) as illustrated in **Figures 2** and **3**. Since this study is focused on the seasonal variability of CCF, monthly maps of GM and FF served as a main instrument in data analysis. We also paid attention to interannual variations; however, the limited length (<6 years) of the AHI dataset precludes a rigorous study of interannual variability, which will become possible after addition of *Himawari-9* data, to be collected over 2022-2030.

Preprints (www.preprints.org) | NOT PEER-REVIEWED | Posted: 9 January 2023 doi:10.20944/preprints202301.0147.v1

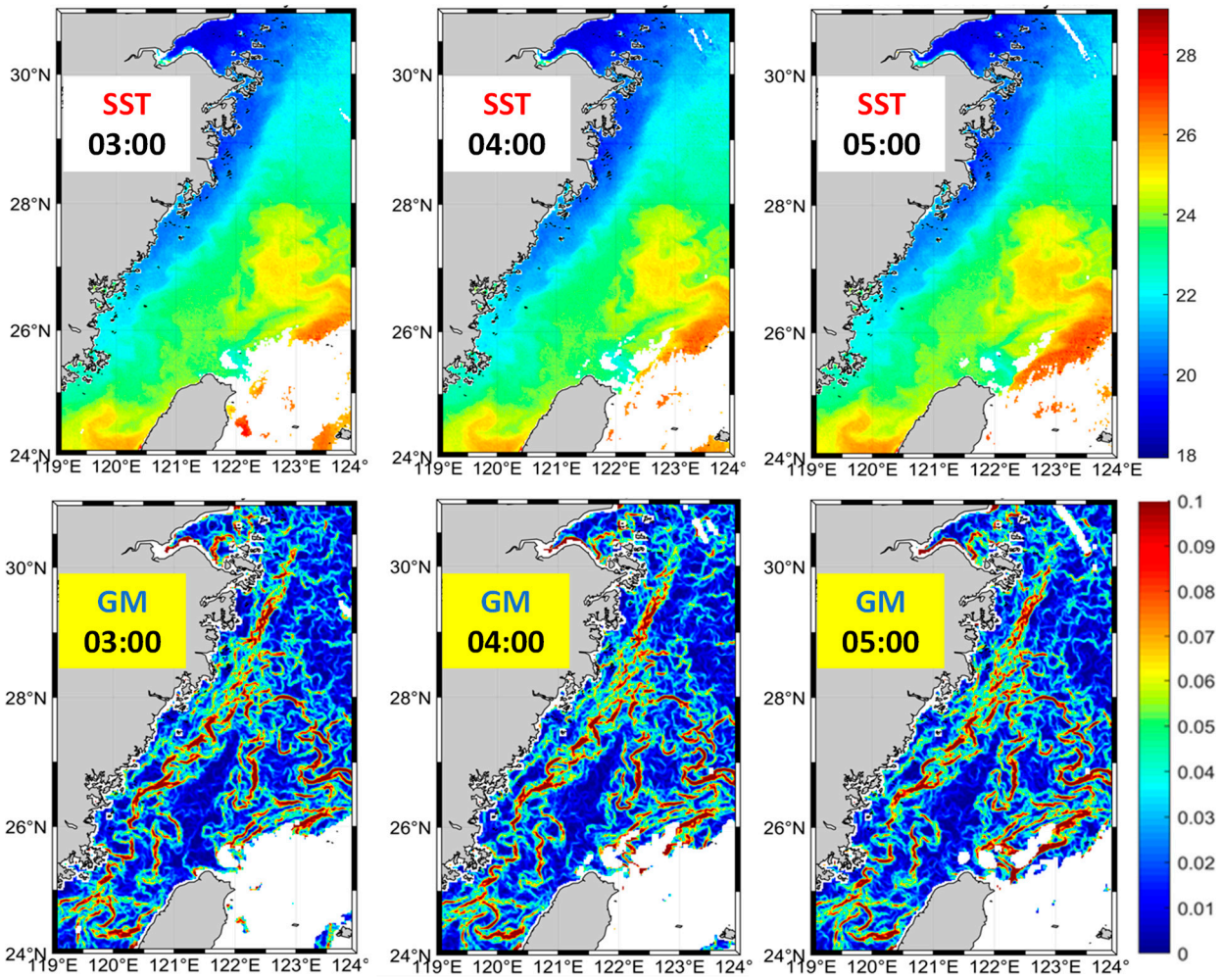

Figure 1. Sample hourly data from 27 October 2018. Top row: SST (°C). Bottom row: SST gradient magnitude GM (°C/km). Offshore fronts, including the CCF and Kuroshio branches, do not change their location, shape, and gradient at the hourly scale, while many inshore shallow fronts vary appreciably over hourly intervals.

Preprints (www.preprints.org) | NOT PEER-REVIEWED | Posted: 9 January 2023 doi:10.20944/preprints202301.0147.v1

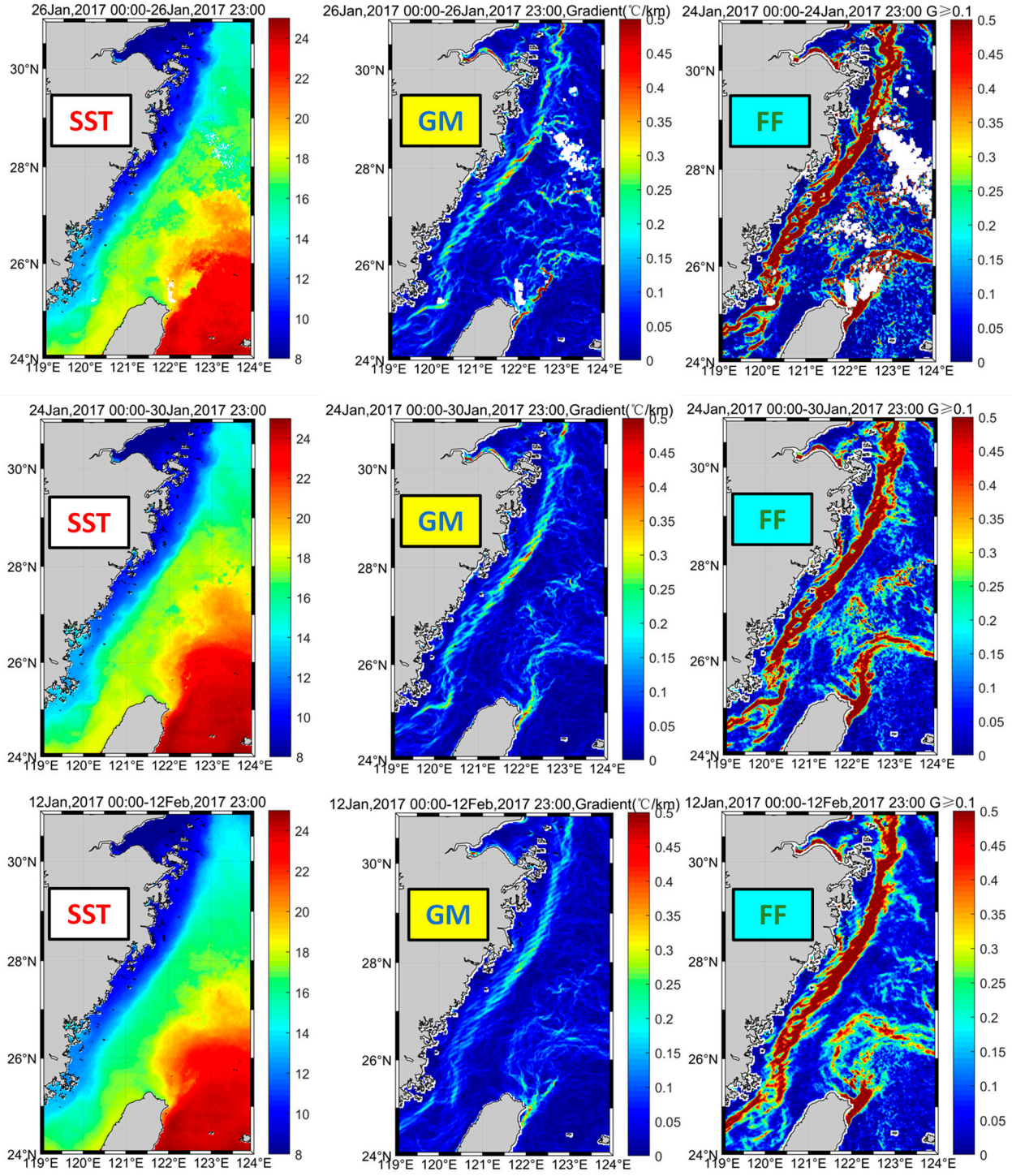

Figure 2. Sample data sets illustrating daily (top row), weekly (middle row) and monthly (bottom row) data. Each data set consists of SST (°C; left), SST gradient magnitude GM (°C/km; center), and frontal frequency FF at GM>=0.1°C/km (right).

Preprints (www.preprints.org) | NOT PEER-REVIEWED | Posted: 9 January 2023 doi:10.20944/preprints202301.0147.v1

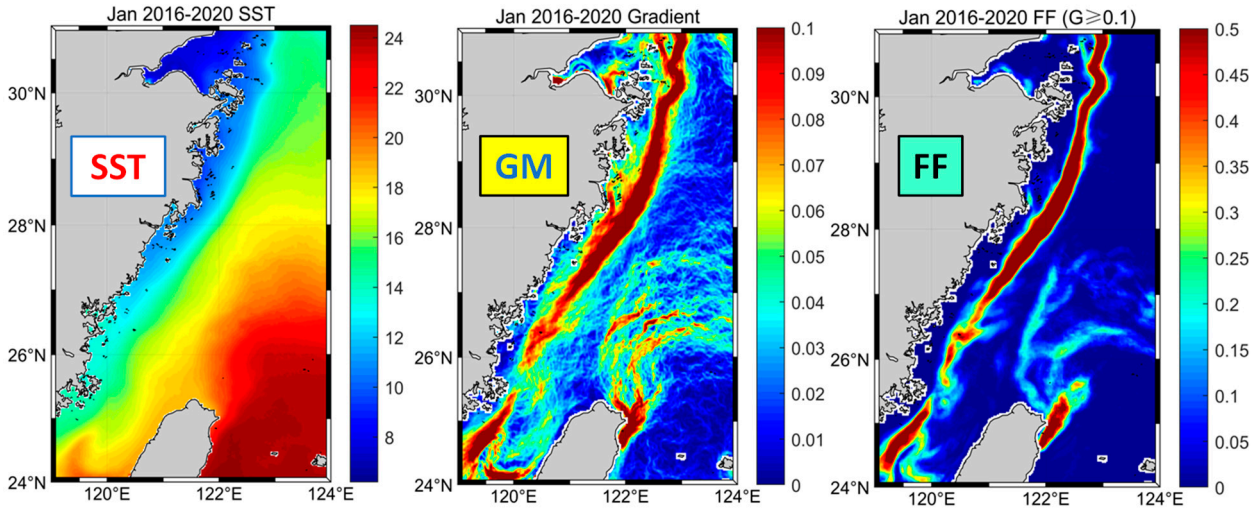

Figure 3. Sample long-term mean data for January 2016-2020. Left: SST (°C). Center: SST gradient magnitude GM (°C/km). Right: Frontal frequency FF at GM>=0.1 °C/km.

3. Results

3.1. Introduction and Main Set of Results

Key parameters of fronts are: (1) *intensity* identified with gradient magnitude GM, (2) *robustness* quantified as pixel-based frontal frequency FF, and (3) *strength* measured as the total cross-frontal range of a frontal variable in question, e.g., SST. The complete set of results includes a collection ("atlas") of frontal maps (166 maps, see Supplementary Materials) that consists of (1) individual monthly maps of gradient magnitude GM and frontal frequency FF (132 maps, covering the study period from July 2015 through December 2020), (2) annual mean maps of GM and FF (2016-2020; 10 maps), and (3) long-term mean monthly maps of GM and FF (24 maps). The Supplementary Materials also include a set of cross-frontal plots of monthly SST along 8 zonal lines at every degree of latitude from 31°N to 24°N. These plots document the downstream variability of the CCF and its seasonal and interannual variabilities. In the below section we present and analyze most important results, namely long-term mean monthly maps of SST (**Figure 4**), GM (**Figure 5**), and FF (**Figure 6**), and plots of SST across the front (**Figures 7** and **8**).

The monthly maps of SST (**Figure 4**) reveal strong seasonal variability of SST in the ECS. Between winter and summer, the SST varies from 7°C to 31°C, spanning a 24-degree temperature range, one of the largest seasonal SST ranges in the World Ocean. These maps also reveal the seasonal emergence and disappearance of the cold CCC offshore the Zhejiang-Fujian coast. The seasonal emergence of the Taiwan Warm Current (TWC) is evident in these maps, albeit not so vividly as the CCC because of a smaller SST contrast between the TWC and coastal waters offshore the Fujian coast in summer, when the TWC is best developed.

Preprints (www.preprints.org) | NOT PEER-REVIEWED | Posted: 9 January 2023 doi:10.20944/preprints202301.0147.v1

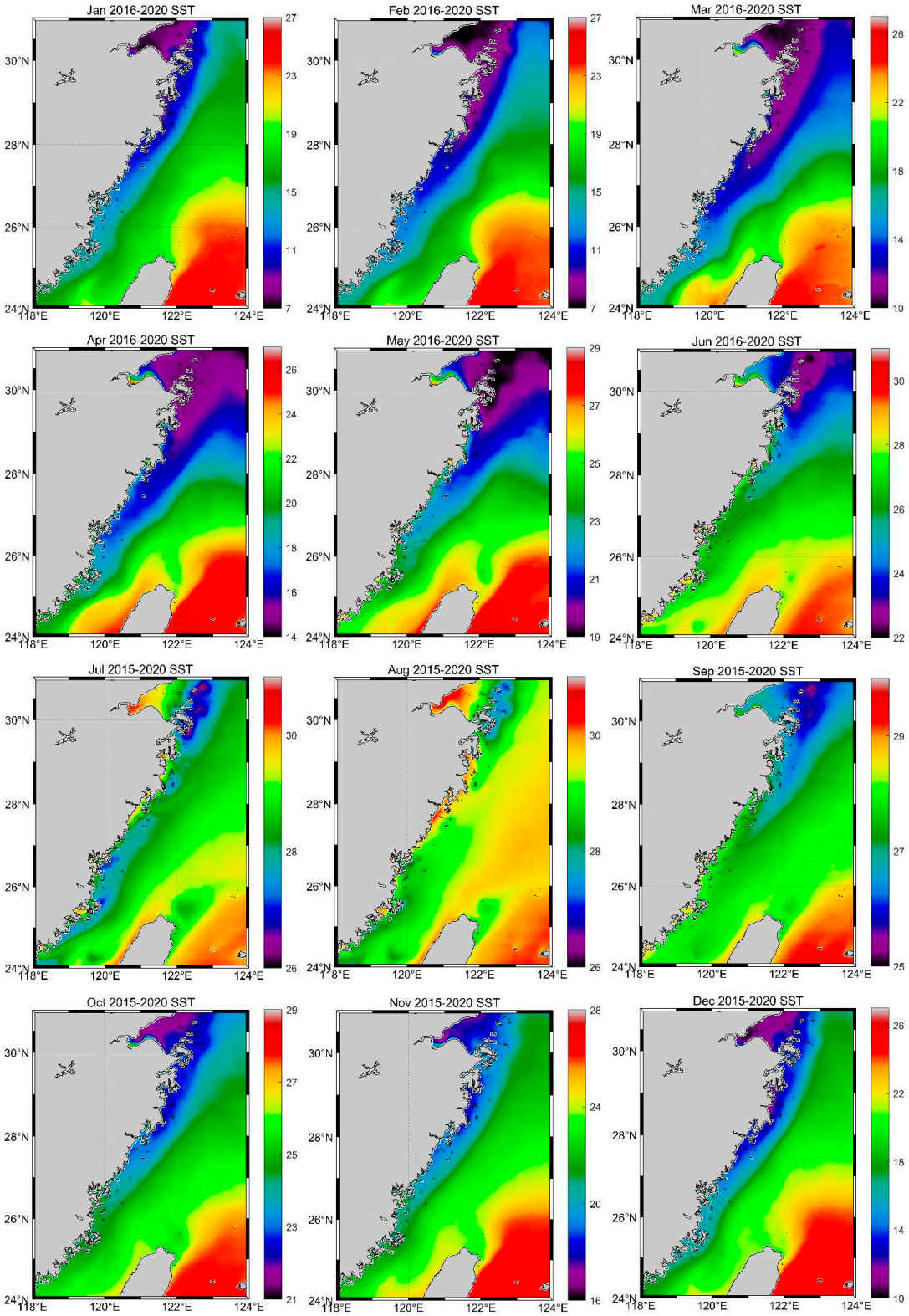

Figure 4. Long-term (2015-2020) mean monthly maps of SST (°C).

Preprints (www.preprints.org) | NOT PEER-REVIEWED | Posted: 9 January 2023 doi:10.20944/preprints202301.0147.v1

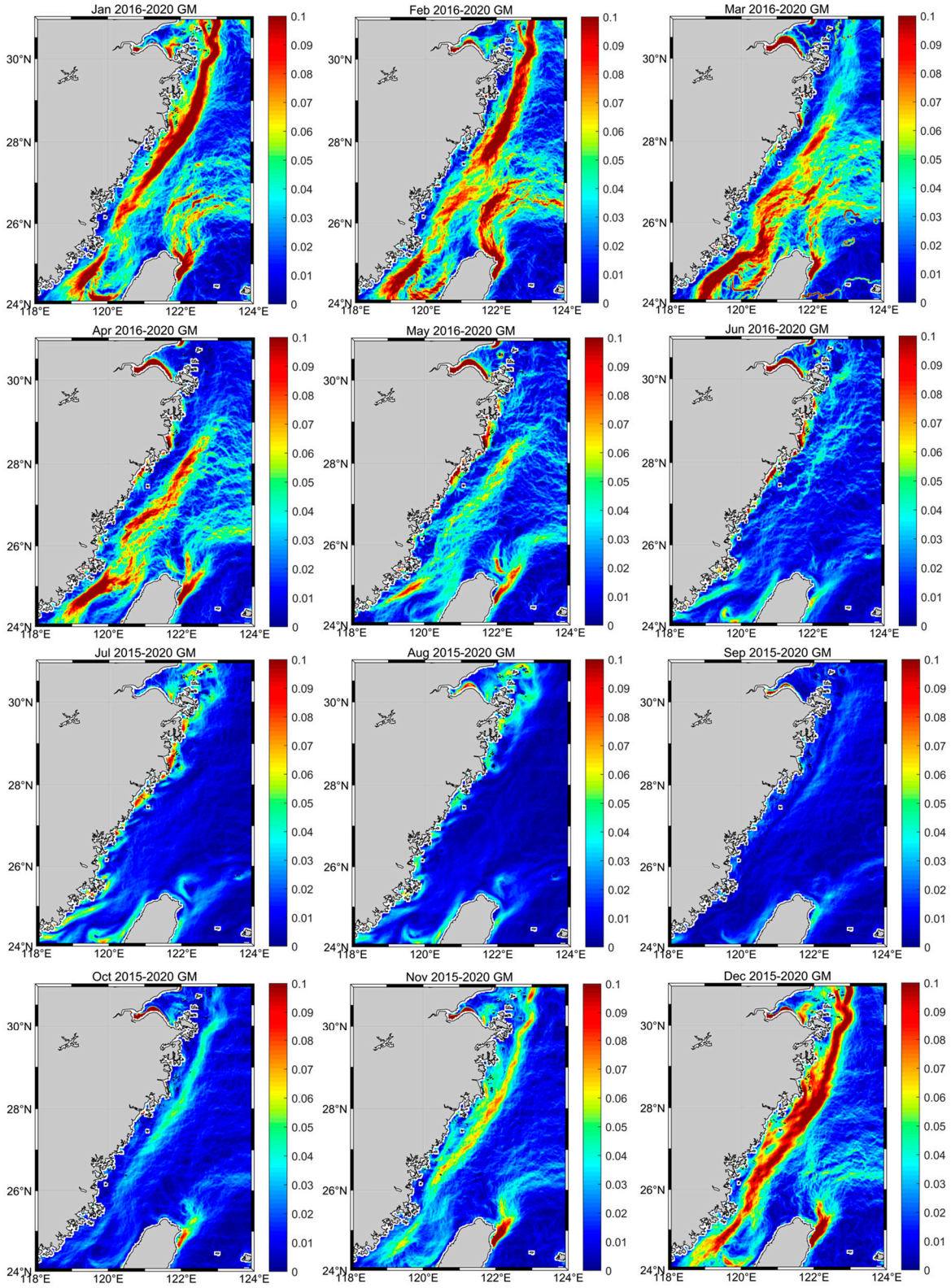

Figure 5. Long-term (2015-2020) mean monthly maps of SST gradient magnitude GM.

Preprints (www.preprints.org) | NOT PEER-REVIEWED | Posted: 9 January 2023 doi:10.20944/preprints202301.0147.v1

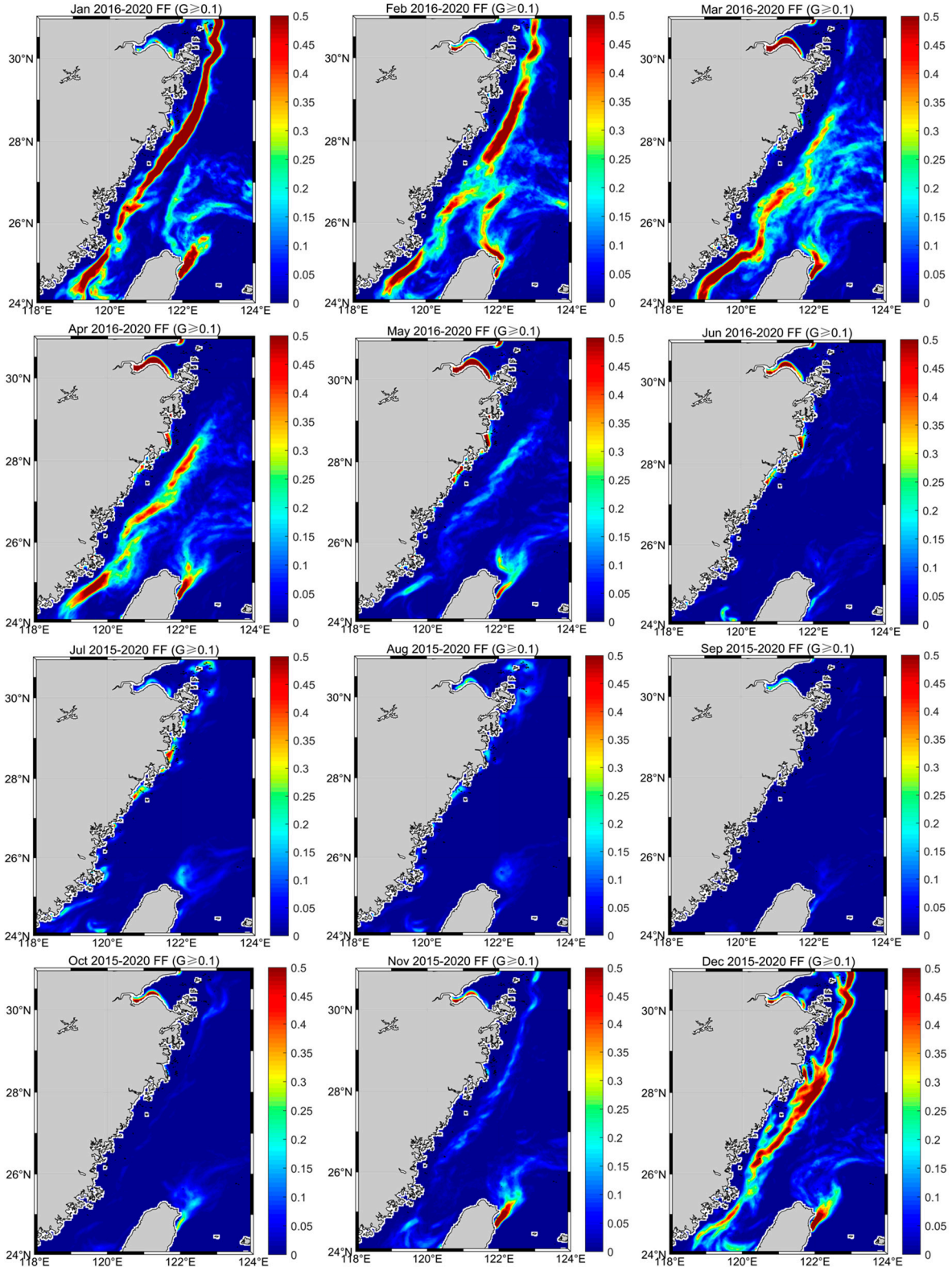

Figure 6. Long-term (2015-2020) mean monthly maps of frontal frequency FF at GM≥0.1°C/km.

Preprints (www.preprints.org) | NOT PEER-REVIEWED | Posted: 9 January 2023 doi:10.20944/preprints202301.0147.v1

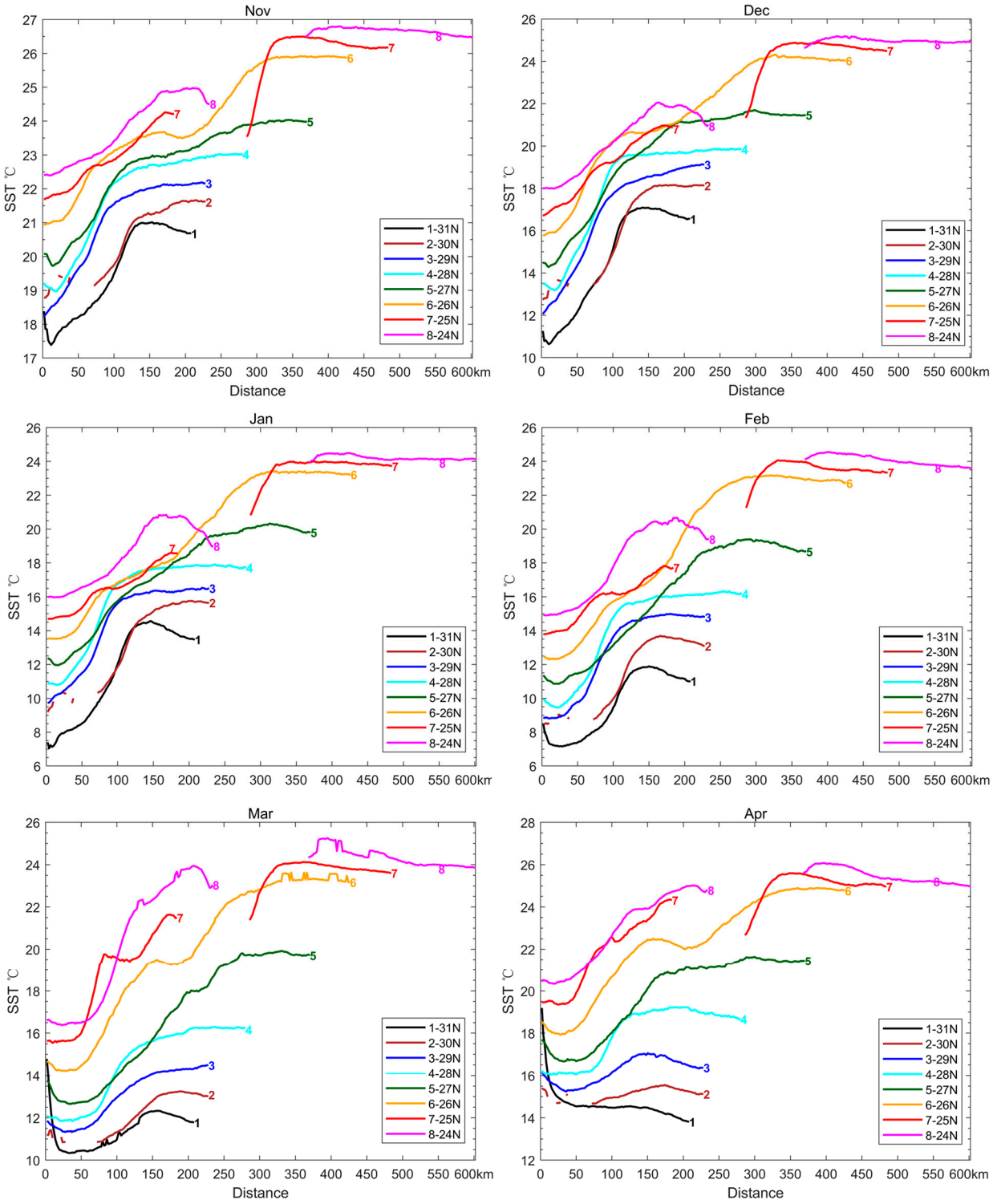

Figure 7. Long-term (2015-2020) mean monthly distributions of SST along 8 zonal lines across the CCF during winter months (November through April).

Preprints (www.preprints.org) | NOT PEER-REVIEWED | Posted: 9 January 2023 doi:10.20944/preprints202301.0147.v1

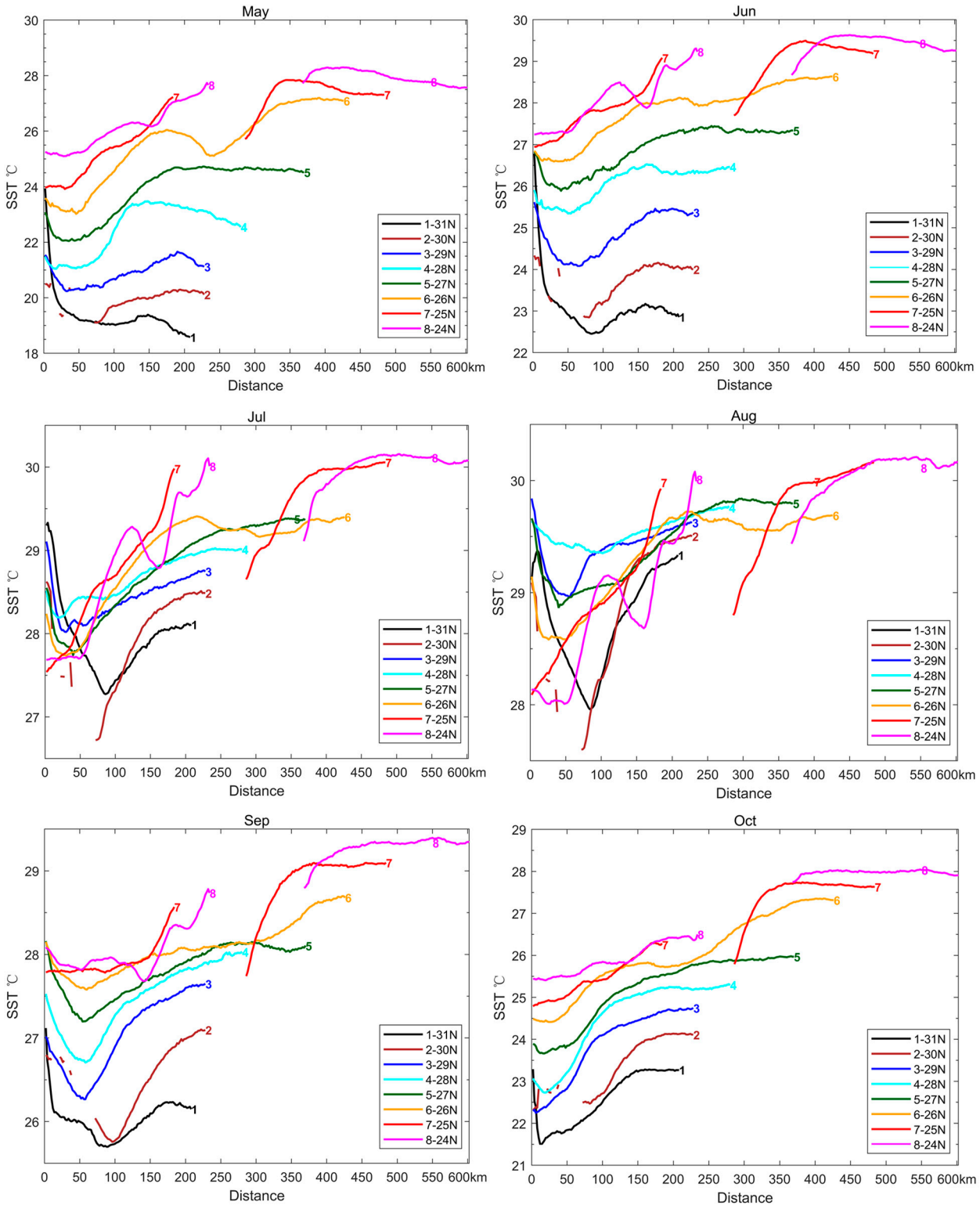

Figure 8. Long-term mean monthly distributions of SST along 8 zonal lines across the CCF during summer months (May through October).

The monthly maps of GM (**Figure 5**) document seasonal variability of the CCF. Consistent with previous studies (Lee et al., 2015), these maps reveal the emergence of CCF, albeit weak and diffuse, in September offshore the Zhejiang coast (27-30°N). The newly formed front is separated from inshore waters by a well-defined gradient trough (GM minimum, a narrow band of near-zero GM) extending over 20-25-m depths in the north and 35-40-m depths in the south. This enigmatic feature is only observed in September. In October, the CCF is formed along the entire Zhejiang-Fujian coast between

Preprints (www.preprints.org) | NOT PEER-REVIEWED | Posted: 9 January 2023 doi:10.20944/preprints202301.0147.v1

the 20-m and 50-m isobaths. From October through February, the front shifts over deeper waters (consistent with Lee et al., 2015) and is best developed in December-February. The front disintegrates from March through June and is absent in July-August. The inshore front observed by He SY et al. (2016) in December-January is noticeable in **Figure 5** from November through February.

The overall pattern of seasonal variability of the CCF according to the monthly maps of frontal frequency FF (at GM≥0.1°C/km) (**Figure 6**) is generally consistent with the CCF's seasonal variability pattern according to the monthly maps of SST gradient magnitude GM (**Figure 5**). The CCF emerges in November, becomes robust in December, and remains robust through February. The transition from the formation stage in November to the mature stage (in terms of frontal robustness) in December occurs in a month and thus seems to be relatively rapid and almost abrupt, especially when other factors are considered, e.g., the sharp cooling of the CCC from November to December as documented by cross-frontal SST plots (**Figures 7** and **8**) discussed below. The CCF disintegrates and shrinks lengthwise in March, although already in February the front is fragmented. The front completely disappears in FF maps from June through October.

To explore cross-frontal structure of SST, we plotted long-term mean monthly SST along 8 parallels from 31°N to 24°N (**Figures 7** and **8**). These "waterfall" plots reveal details of cross-frontal structure of SST field that may go unnoticed in maps of SST (**Figure 4**), GM (**Figure 5**), and FF (**Figure 6**). The waterfall plots also allow to accurately evaluate cross-frontal SST steps dSST defined as a difference between offshore and inshore SST: dSST=Offshore SST – Inshore SST. Obviously, the accurate determination of cross-frontal step is critically dependent on the accurate determination of offshore and inshore SST, which in turn is critically dependent on the accurate identification of the offshore and inshore boundaries of the front in question.

In a classical concept of a front, cross-frontal distributions of oceanic variables, e.g., SST, are described by a smooth, twice differentiable function of cross-frontal distance. This is a very crude approximation, in which frontal boundaries do not exist. This concept was born out of traditional in situ measurements at oceanographic stations separated by tens or even hundreds of kilometers. The picture of the ocean based on such sparse data was smooth. In this picture, ocean fronts appeared as gradual transition zones rather than stepwise boundaries. We know now that traditional widely separated observations could not reveal true horizontal structure of most fronts.

Over the last 50 years, accumulation of underway high-resolution in situ measurements of oceanic variables as well as high-resolution remote sensing observations from aircraft and satellites revealed horizontal structure of numerous fronts that can be approximated by a ramp function (Belkin and O'Reilly, 2009). In this model, frontal boundaries are defined as points of maximum curvature. Close examination of cross-frontal SST plots in **Figures 7** and **8** shows that in most cases such points can be identified with confidence. In other cases, the maximum curvature method does not work; in such cases, the boundaries are identified as points where SST reaches a plateau; these plateaus correspond to the SSTs of water masses separated by the front.

It should be stressed that the plots in **Figures 7** and **8** are based on long-term mean SST data that are smoothed by averaging. Fortunately, owing to the steering (front-controlling) effect of local topography, the CCF position is relatively stable; therefore, the smearing (smoothing) effect of long-term averaging is not as detrimental as it could be otherwise.

3.2. China Coastal Front during Cold Seasons (November through April)

The SST plots in **Figure 7** were used to determine long-term mean monthly SST ranges (cross-frontal SST steps) across the CCF along eight zonal lines from 31°N to 24°N during cold seasons (November through April) (**Table 2**). The monthly SST ranges in **Table 2** document both spatial and temporal variability of the CCF. First, these data show how the CCF strength changes downstream from offshore the Hangzhou Bay down to the Taiwan Strait. Second, these data document the seasonal waxing and waning of the CCF during the cold seasons.

Preprints (www.preprints.org) | NOT PEER-REVIEWED | Posted: 9 January 2023 doi:10.20944/preprints202301.0147.v1

Table 2. Long-term (2016-2020) mean monthly SST across the CCF along 8 parallels (from 31°N to 24°N) during cold seasons. In each pair of numbers, the first/second number is SST (°C) at the front's inshore/offshore boundary, respectively. All SST values are rounded to the nearest half-degree. Color codes are used for SST range dSST=Offshore SST–Inshore SST. Color scale: yellow means dSST between 3°C and 3.5°C; green, 4.0-4.5°C; blue, 5.0°C and higher.

Latitude	November	December	January	February	March	April
31°N	17.5-21.0	11.0-17.0	7.0-14.5	7.0-12.0	10.5-12.5	19.0-14.5
30°N	19.0-21.0	13.0-18.0	10.0-14.5	9.0-13.5	11.0-13.0	14.5-15.5
29°N	18.5-21.5	12.0-18.0	10.0-16.0	9.0-15.0	11.5-14.0	15.5-17.0
28°N	19.0-22.0	13.0-19.5	11.0-16.5	9.5-15.5	12.0-15.5	16.0-19.0
27°N	20.0-22.5	14.5-21.0	12.0-17.0	11.0-18.5	12.5-18.0	16.5-21.0
26°N	21.0-22.5	16.0-20.5	13.5-16.5	12.5-15.5	14.5-19.0	18.0-22.5
25°N	21.5-22.5	17.0-19.0	14.5-16.5	14.0-16.0	15.5-19.5	19.5-22.5
24°N	22.5-25.0	18.0-22.0	16.0-21.0	15.0-20.0	16.5-22.0	20.5-24.0

Main conclusions from **Table 2** can be summarized as follows:

(1) The CCF is the strongest in winter (December through February) when dSST=5°C and higher (blue cells), up to 7.5°C, along the entire Zhejiang coast (27-31°N).

(2) The CCF's formation stage in November-December takes approximately one month, during which dSST increases sharply (from 3.0°C to >6.0°C) owing largely to the sharp decrease of the inshore SST (by 6.0-6.5°C).

(3) The CCF's weakening begins in March. The weakening is most pronounced off the Zhejiang coast, where dSST drops from 6.0°C in February to 2.0-3.5°C in March. The sharp weakening of the CCF off the Zhejiang coast is caused by rapid increase of the inshore SST.

(4) The CCF's springtime warming is the most rapid between March and April, when the inshore/offshore SST increases by 4.0°C/3.5°C, respectively.

(5) The anomalously high offshore SST at 27°N is notable from December through March, with a peak in February-March.

(6) The anomalously high inshore SST at 31°N in April (19.0°C!) is likely caused by an influx of relatively warm waters diluted by spring freshets from the Yangtze River and Hangzhou Bay.

3.3. China Coastal Front during Warm Seasons: Summer Upwelling

During warm seasons (May-October or "summer" hereafter), the CCF appearance in SST is fundamentally different from the front's appearance during cold seasons ("winter" hereafter), when SST monotonously increases in the offshore direction (**Figure 7**). In summer, the cross-front distribution of SST is non-monotonous (**Figure 8**). Instead, as a rule, the SST features a well-defined minimum at some distance from the shore. This cold water is brought to the sea surface by upwelling. The spatial SST patterns in winter and summer are illustrated by **Figure 9**, where the winter SST distribution in the offshore direction is approximated by the ramp model, while the summer SST distribution is approximated by the valley model (V-shaped or U-shaped).

Preprints (www.preprints.org) | NOT PEER-REVIEWED | Posted: 9 January 2023 doi:10.20944/preprints202301.0147.v1

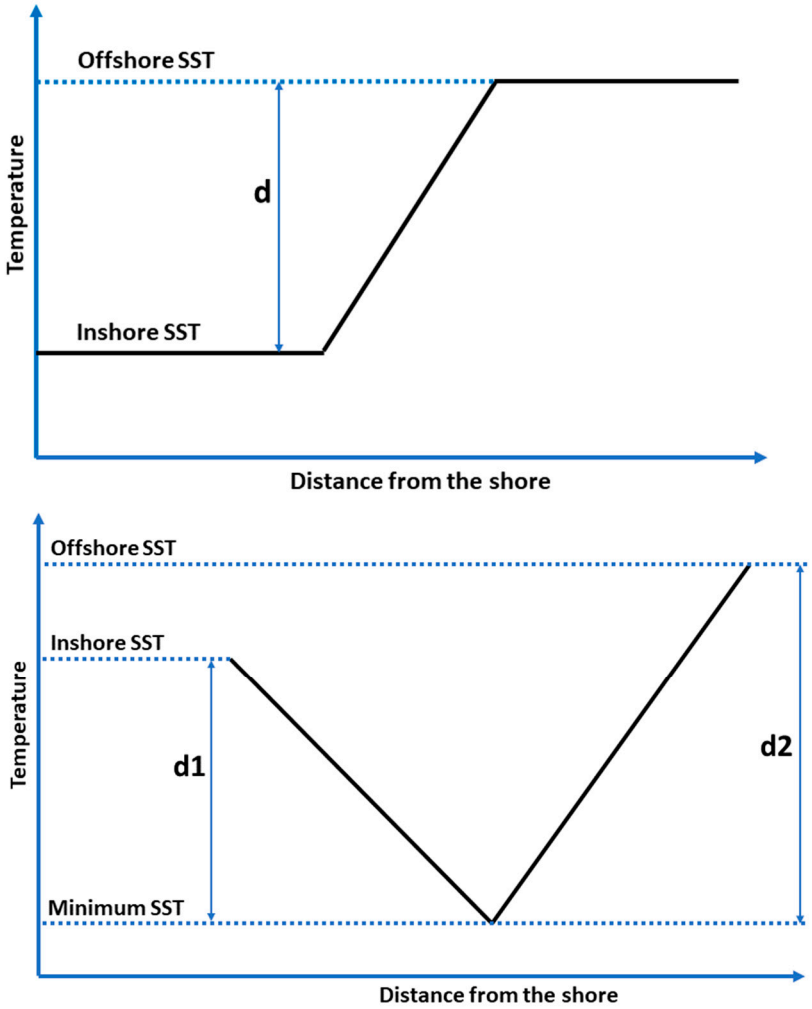

Figure 9. Ramp model (top) vs. valley model (bottom). **d**, Offshore SST – Inshore SST; d1, Inshore SST – Minimum SST; **d2**, Offshore SST – Minimum SST.

The V-shaped and U-shaped patterns of SST distribution across the summer upwelling off the Zhejiang and Fujian coasts are evident from satellite SST imagery. Such patterns have been noted in previous studies by our predecessors. Hu and Zhao (2008) provided examples of V-shaped (*ibid.*, Figure 4a) and U-shaped (*ibid.*, Figure 4b) SST patterns off the Zhejiang coast along, respectively, 31.5°N and 30.2°N parallels. Lou XL et al. (2011) provided an example of U-shaped pattern off the Zhejiang coast along the 30.5°N line (*ibid.*, Figure 4) and noted: "There exists obvious temperature front between the upwelling waters and its surrounding non-upwelling waters. The temperature differences between the two types of waters can be greater than 2℃, and the temperature gradient can even reach to 0.1℃/km." Thus, Lou XL et al. (2011) recognized the existence of ***two fronts*** on the opposite sides of the upwelled water. The V-shaped and U-shaped SST patterns are apparent in cloud-free satellite SST imagery, which is advantageous vs. ship surveys that cannot be safely conducted in shallow waters off the Zhejiang and Fujian coasts dotted with myriads of islands and other navigational hazards. For example, two dedicated multi-cruise surveys of the Zhejiang summer upwelling reported by Pan et al. (1987) had to avoid shallow waters of the inner shelf with depths less than ~20 m (*ibid.*, Figure 1).

Using SST data shown in **Figure 8**, we determined minimum SST along each of 8 zonal sections during each month (**Table 3**).

Preprints (www.preprints.org) | NOT PEER-REVIEWED | Posted: 9 January 2023 doi:10.20944/preprints202301.0147.v1

Table 3. Minimum SST (°C) during warm seasons.

Latitude	May	Jun	Jul	Aug	Sep	Oct
31°N	19.0	22.5	27.3	28.0	25.7	21.5
30°N	19.1	22.8	26.7	27.6	25.8	22.3
29°N	20.3	24.1	28.0	29.0	26.3	22.3
28°N	21.0	25.4	28.2	29.3	26.7	22.8
27°N	22.0	25.9	27.8	28.9	27.2	23.7
26°N	23.0	26.7	27.7	28.6	27.6	24.5
25°N	24.0	27.0	27.5	28.1	27.8	24.8
24°N	25.1	27.3	27.7	28.0	27.8	25.5

Comments on Table 3:

(1) At each latitude, seasonal variations of min SST are apparent. The magnitude of seasonal change of min SST decreases with latitude decreasing: From May to August, at 31°N the min SST increases by 9°C (from 19.0 to 28.0°C), yet at 24°N the min SST increases by only 3°C (from 25.1 to 28.0°C).

(2) Downstream trends between 31°N and 24°N are dramatically different in spring (May) and autumn (Oct) vs. summer's peak (July-August). The min SST increases downstream by 6°C in May and 4°C in October, whereas in July-August the min SST is uniform spatially (between 31°N and 24°N) and temporally (for two months), remaining within a 2°C range (27-29°C).

The magnitude of summer upwelling can be assessed using various approaches. In our case, two simple parameters that can be easily computed are *inshore and offshore SST ranges* defined as follows: Inshore Range=Inshore SST – Min SST and Offshore Range=Offshore SST – Min SST. These two parameters are presented in **Table 4** (Offshore Range) and **Table 5** (Inshore Range).

Table 4. Offshore SST – Minimum SST (°C) during warm seasons.

Latitude	May	Jun	Jul	Aug	Sep	Oct
31°N	0.4	0.8	0.8	1.3	0.6	1.8
30°N	0.6	1.4	1.8	1.7	1.3	1.6
29°N	0.7	1.3	0.8	0.4	1.5	1.8
28°N	2.4	1.2	0.8	0.5	1.3	2.1
27°N	2.7	1.5	1.6	0.9	0.9	1.8
26°N	3.0	1.4	1.7	1.1	0.4	1.4
25°N	1.5	0.9	1.2	1.8	0.7	0.6
24°N	1.2	1.2	1.6	1.2	0.6	0.4

Comments on Table 4:

(1) The maximum difference Offshore SST – Min SST is observed in May (2.4-3.0°C between 26-28°N), not at the peak of summer upwelling (July-August) as expected. The most plausible explanation is that in May the China Costal Current still persists, bringing relatively cold waters southward along the Zhejiang-Fujian coast.

(2) Except for May, the Offshore SST – Min SST difference remains below 2.1°C, often dropping below 1°C. These relatively low numbers can be explained by the intermittent nature of wind-

Preprints (www.preprints.org) | NOT PEER-REVIEWED | Posted: 9 January 2023 doi:10.20944/preprints202301.0147.v1

driven coastal upwelling and long-term averaging used to generate mean monthly SST data in this study.

Table 5. Inshore SST – Minimum SST (°C) during warm seasons.

Latitude	May	Jun	Jul	Aug	Sep	Oct
31°N	5.0	4.3	2.1	1.3	1.3	1.5
30°N	1.5	1.5	2.0	0.5	1.3	1.0
29°N	1.3	1.4	1.1	0.8	0.8	0.0
28°N	0.5	0.5	0.3	0.4	0.8	0.3
27°N	1.0	1.0	0.8	0.9	0.8	0.2
26°N	0.5	0.3	0.5	0.5	0.5	0.1
25°N	0.0	0.0	0.0	0.0	0.0	0.0
24°N	0.1	0.0	0.0	0.1	0.2	0.0

Comments on Table 5:

(1) Extremely high values of the Inshore SST – Min SST difference at 31°N in May-June are partly explained by an influx of warm waters from the Hangzhou Bay and Yangtze River due to heavy rains during the Mei-Yu season (late spring – early summer).

(2) Farther south, the Inshore SST – Min SST difference gradually decreases down to 0 at 24-25°N. This means that upwelled waters spread up to the coast -- or very near the coast -- of southern Fujian. Elsewhere along the Zhejiang-Fujian coast, cold upwelled waters do not spread up to the shore, thereby leaving some space for warmer inshore waters.

4. Discussion

4.1. Summary

The results presented in the previous section document both spatial and temporal variability of the CCF. The most important aspect of spatial variability is the downstream evolution of the CCF. We documented the downstream variability of key parameters of the front: its intensity GM (cross-frontal SST gradient magnitude) and strength dSST (Offshore ST – Inshore SST). The variability of the front's location is characterized by pixel-based frontal frequency FF.

The most important scale of temporal variability is the seasonal evolution of the CCF. Our results on the seasonal variability of the front's transversal structure in SST are suggestive of the front changing its physical nature from winter to summer. In winter, the CCF is a water mass front maintained by the southward flow of cold and fresh China Coastal Current. In summer, the CCF is an upwelling front maintained by the seasonally dominant southwesterlies.

4.2. Spatial Variability

The origin of the China Coastal Current and associated front can be traced back to the northern Yellow Sea. During the winter monsoon, the prevailing northerly winds (caused by the Siberian anticyclone ("Siberian High") drive the southward current along the Shandong and Jiangsu (Subei) coasts. This current is commonly called the Yellow Sea Cold Current (YSCC). The YSCC can be considered as the origin (or precursor) of the China Coastal Current. Farther south, the YSCC encounters the Yangtze River Plume (YRP), which spreads in a general eastward direction, although sometimes, especially in winter, the plume is deflected to the southeast. Any interaction between the YSCC and YRP is bound to be complicated and subject to strong temporal variability, modulated by the intrinsic variability of the Yangtze River discharge. Therefore, the fate of YSCC remains a matter

of debate and a focus of numerous studies. In particular, it is not clear, what is the contribution of the YSCC to the CCC farther south. It is quite possible that the entire YSCC (or, at least, the bulk of it) recirculates within the Yellow Sea, so that the amount of YSCC water that escapes south is insignificant. South of the Yangtze Shoal, the China Coastal Current flows past the Hangzhou Bay and along the Zhejiang-Fujian coast. The CCC eventually extends into the Taiwan Strait, possibly (at least, occasionally) flowing along the Guangdong Coast.

The CCC and associated front (CCF) are steered by shallow bathymetry (topography) of the Zhejiang-Fujian shelf. Numerous studies of the CCC determined that the CCC flows over the inner shelf with depths in the 20-60 m range. Our study confirmed this depth range for the CCF. We also found that the front shifts to deeper waters, from <20 m to >50 m, as the season progresses. This seasonal trend can be noticed in the results presented by Lee et al. (2015, Figure 3C), although Lee at al. (2015) have not commented on this seasonal trend.

The front's continuity along the Zhejiang-Fujian coast is not a given, even in winter, when all three key frontal parameters peak, namely the front's sharpness (intensity defined as gradient magnitude GM), stability (robustness identified with front frequency FF), and strength (cross-front range dSST). During the 2015-2020 study period, we observed a few breakdowns of the front as documented by individual monthly maps of GM (Supplementary Information). It happened in February 2016, then again (but stronger) in February 2017, then again (yet weaker) in January-February 2018, then stronger again in February 2019, and then again in January-February 2020. In winter 2019-2020, the front's continuity throughout the study area (24-31°N) was not fully established as evidenced by monthly maps for December 2019 and January-February 2020.

Local breaks of the front can be expected off of major promontories and islands, as well as over submarine topographic highs such as banks or shallows. The most notable quasi-regular breakdown of the front occurs near 27°N in winter (January-February). Another area where breakdown occurs each year, also in winter, is near 25.5°N. Both breakdowns are evident in monthly maps of GM and FF (**Figures 5** and **6**). These breakdowns manifest as short segments of the front with lower GM and lower FF. The quasi-stationary localization of these breakdowns suggest topographic control. The spatially localized breakdowns of the front at 27°N and 25.5°N occur in winter only. The most likely explanation of the distinct seasonality of these breakdowns involves the front's interaction with bathymetry. This interaction intensifies in winter owing to the seasonal wintertime deepening of the front that leads to a stronger interaction of the front with the underlying topographic features.

Inshore fronts off the Zhejiang coast (between the CCF and coast) are evident in the November, December, and January maps of GM (**Figure 5**). These fronts (or a single front that may consist of a few segments connected/disconnected to/from one another) have been identified by He SY et al. (2016) and are noticeable in Lee et al. (2015, Figures 2 and 3). Our monthly maps of FF (**Figure 6**) show a persistent inshore front at 28°N. This feature is the most robust fragment of the inshore front, whose enhanced stability is most likely explained by the steering effect of local bathymetry.

4.3. Seasonal Variability

The CCC and CCF exhibit strong seasonal variations that are largely driven by seasonally reversing monsoons. The impact of the winter monsoon driven by the Siberian High is crucial in establishing the southward China Costal Current and CCF. The winter monsoon-driven transition in the ECS is completed in December, which is relatively early compared to the distant offshore North Pacific where oceanic seasons generally lag respective terrestrial seasons by a month. The early winter development of the CCC and CCF is explained by the ECS proximity to Siberia with its sharply continental climate. The winter climate in the YECS region is strongly affected by northerly winds driven by the Siberian High. Therefore, the winter climate in the YECS region is synchronized with the terrestrial climate in Siberia.

The front is best defined during the winter monsoon, when the front's sharpness (GM) and strength (dSST) peak in January-February. From March onward, the front gradually changes its physical nature: From a typical water mass front between cold, fresh waters of the CCC and warm, saline offshore waters, the front evolves into a typical wind-driven coastal upwelling front

Preprints (www.preprints.org) | NOT PEER-REVIEWED | Posted: 9 January 2023 doi:10.20944/preprints202301.0147.v1

maintained by the southerlies during the summer monsoon. Oceanographic surveys and numerical modeling show that upwelling off the Zhejiang-Fujian coast exist year-round, with summer upwelling being much stronger than winter upwelling (Qiao FL et al., 2006). Therefore, the discussion below is focused on summer upwelling.

The summer monsoon-driven southerly winds blowing along the Zhejiang-Fujian coast cause upwelling that is best defined in the *southern* East China Sea, starting in March-April between 24-27°N as evidenced by maps of SST (**Figure 4**), GM (**Figure 5**), and FF (**Figure 6**), zonal plots of SST (**Figure 8**), and tables with summer upwelling parameters, including minimum SST (**Table 3**), upwelling's offshore magnitude (**Table 4**), and upwelling's inshore magnitude (**Table 5**).

4.4. Comments on Previous Satellite Studies of SST Fronts off the Zhejiang-Fujian Coast

Previous satellite studies have elucidated many aspects of spatial and temporal variability of SST fronts off the Zhejiang-Fujian coast, particularly in winter (**Table 6**). A cautionary remark is warranted regarding any comparison of quantitative frontal parameters such as, e.g., gradient magnitude (GM) and frontal frequency (FF). It's well known that estimates of GM depend on data resolution, with poor resolution resulting in low GM. Data averaging in time domain (which is sometimes necessary to mitigate data gaps caused by cloudiness) also results in artificially low GM. Frontal frequency (FF) is derived differently in histogram-based algorithms such the Cayula-Cornillon (1992) algorithm (CCA) and gradient-based algorithms such as the Belkin and O'Reilly (2009) algorithm (BOA). In the CCA, frontal frequency FF is defined and computed independently from GM. In the BOA (and similar algorithms), frontal frequency FF is computed based on a GM threshold so that any pixel with GM exceeding the threshold is declared a frontal pixel that is a pixel that contains a fragment of a front. The choice of GM threshold is arbitrary as there is no physically based algorithm for threshold selection. Usually, GM threshold is selected after trial-and-error experiments with various thresholds.

Table 6. Satellite studies of SST fronts off the Zhejiang-Fujian coast GM, gradient magnitude; FF, frontal frequency.

Reference	Data Resolution (km)	GM Threshold (°C/km)	Main Products Published
Belkin et al. (this study)	2	0.1	Monthly maps of GM and FF
Cao L et al. 2021	4	0.014	Seasonal maps of FF
Chang et al. 2006	1.1	Not used	Winter maps of FF (Dec.-Feb.)
Chang et al. 2008	1.1	Not used	Winter maps of FF (Dec.-Feb.)
Chang et al. 2010	1.1	Not used	Winter maps of FF (Dec.-Mar.)
He SY et al. 2016	4	0.1	Winter maps of FF (Nov.-Feb.)
Hickox et al. 2000	9	Not used	Seasonal maps of FF
Huang et al. 2010	6-22	0.05	Monthly maps of GM and FF
Lee et al. 2015	1.1	Not used	Monthly maps of GM
Liu DY et al. 2018	4	Not used	Monthly maps of GM
Pi and Hu 2010	5	Not used	Monthly maps of GM
Ping et al. 2016	4	Not used	Monthly maps of GM
Qiao LL et al. 2020	1	Not used	Annual winter maps of GM
Wang YC et al. 2018	1.1	Not used	Winter maps of GM (Dec.-Mar.)
Zhao et al. 2022	28	Not used	Monthly maps of FF

5. Summary and Conclusions

High-resolution (2 km) high-frequency (hourly) SST data from 2015-2020 provided by the Advanced Himawari Imager (AHI) onboard the Japanese *Himawari-8* geostationary satellite positioned over 140.7°E were used to study spatial and temporal variability of the China Coastal Current Front (CCF) in the East China Sea. The hourly SST data were processed with the Belkin and O'Reilly (2009) algorithm (BOA) to generate long-term mean monthly maps of SST gradient magnitude (GM) and frontal frequency (FM) using a GM threshold of 0.1°C/km. Horizontal structure of SST field in the vicinity of the CCF was investigated from cross-frontal distributions of SST along 8 parallels from 31°N to 24°N. The 2-km resolution monthly distributions of SST along these 8 parallels were used to determine inshore and offshore boundaries of the CCF and calculate the CCF strength as a total cross-frontal SST step dSST defined as a difference between the offshore and inshore SST. The CCF emerges in November, fully develops in December and peaks in strength in January-February. The front's fragmentation and shrinking/weakening begins in February and March, respectively. In winter (December-February), the front's strength dSST exceeds 5°C offshore the Zhejiang-Fujian coast and could be as high as 7.5°C, while the inshore SST drops down to 7°C. In winter, the front's strength decreases downstream from 31°N to 24°N.

The CCF changes its physical nature as the seasons progress. In winter, the CCF is a classical water mass front between cold and fresh water coming from the north and warm and salty water coming from the south. In summer, the CCF becomes a coastal upwelling front maintained largely by southerly winds. In winter, the CCF's cross-frontal structure in the SST field is ramp-shaped, with SST increasing monotonously in the offshore direction. In summer, the CCF's cross-frontal structure in the SST field is V-shaped or U-shaped, featuring a minimum SST formed by cold upwelled water at some distance from the shore. Thus, the summer SST structure effectively consists of two fronts, a nearshore and offshore, with a minimum SST in-between. Across the inshore/offshore front, the SST decreases/increases in the offshore direction.

The local topography, especially the steep slope of the inner shelf between 20-m and 50-m isobaths, steers the front. Owing to the topographic steering, the front does not meander in winter off the Zhejiang-Fujian coast. As the cold season progresses, the front gradually shifts into deeper waters, from ~20 m to ~50 m.

Supplementary Materials: The following supporting information can be downloaded at the website of this paper posted on Preprints.org. Individual monthly maps of SST gradient magnitude GM and frontal frequency FF from July 2015 through December 2020.

Author Contributions: I.M.B.: Conceptualization, methodology, data analysis, and writing; W.-B.Y.: Discussions and writing; S.-S.L.: Data curation, processing, visualization, discussions, and writing.

Funding: Shang-Shang Lou and Wenbin Yin were funded by the National Natural Science Foundation of China, grant number 41906025.

Data Availability Statement: No new data were created or analyzed in this study.

Acknowledgments: The Japanese Space Exploration Agency (JAXA) is gratefully acknowledged for making the Himawari-8 AHI data freely available. We are very grateful to Dr. Lei Lin of the Shandong University of Science and Technology for providing a Matlab code of the BOA algorithm. While working on this paper, Igor Belkin was supported by the Zhejiang Ocean University.

Conflicts of Interest: The authors declare no conflict of interest.

References

1. Belkin IM, 2021. Remote sensing of ocean fronts in marine ecology and fisheries. *Remote Sensing* **13** (5), Article number 883. https://doi.org/10.3390/rs13050883.
2. Belkin IM, O'Reilly JE, 2009. An algorithm for oceanic front detection in chlorophyll and SST satellite imagery. *Journal of Marine Systems* **78** (3), 317-326. https://doi.org/10.1016/j.jmarsys.2008.11.018.
3. Bessho K, Date K, Hayashi M, Ikeda A, Imai T, Inoue H, Kumagai Y, Miyakawa T, Murata H, Ohno T, Okuyama A, Oyama R, 2016. An introduction to Himawari-8/9 — Japan's new-generation geostationary meteorological satellites. *Journal of the Meteorological Society of Japan* **94** (2), 151-183. https://doi.org/10.2151/jmsj.2016-009.
4. Cao C, Cai F, Zheng YL, Wu CQ, Lu HQ, Bao JJ, Sun Q, 2018. Temporal and spatial characteristics of sediment sources on the southern Yangtze Shoal over the Holocene. *Scientific Reports* **8** (11), Article 15577. https://doi.org/10.1038/s41598-018-33757-5.
5. Cao L, Tang R, Huang W, Wang YT, 2021. Seasonal variability and dynamics of coastal sea surface temperature fronts in the East China Sea. *Ocean Dynamics* **71**, 237-249. https://doi.org/10.1007/s10236-020-01427-8.
6. Castelao RM, Wang YT, 2014. Wind-driven variability in sea surface temperature front distribution in the California Current System. *Journal of Geophysical Research: Oceans* **119** (3), 1861-1875. https://doi.org/10.1002/2013JC009531.
7. Cayula JF, Cornillon P, 1992. Edge detection algorithm for SST images. *Journal of Atmospheric and Oceanic Technology* **9** (1), 67-80. https://doi.org/10.1175/1520-0426(1992)009<0067:EDAFSI>2.0.CO;2.
8. Chang Y, Shimada T, Lee MA, Lu HJ, Sakaida F, Kawamura H, 2006. Wintertime sea surface temperature fronts in the Taiwan Strait. *Geophysical Research Letters* **33** (23), L23603. https://doi.org/10.1029/2006GL027415.
9. Chang Y, Lee MA, Shimada T, Sakaida F, Kawamura H, Chan JW, Lu HJ, 2008. Wintertime high-resolution features of sea surface temperature and chlorophyll-*a* fields associated with oceanic fronts in the southern East China Sea. *International Journal of Remote Sensing* **29** (21), 6249-6261. https://doi.org/10.1080/01431160802175462.
10. Chang Y, Shieh WJ, Lee MA, Chan JW, Lan KW, Weng JS, 2010. Fine-scale sea surface temperature fronts in wintertime in the northern South China Sea. *International Journal of Remote Sensing* **31** (17), 4807-4818. https://doi.org/10.1080/01431161.2010.485146.
11. Chen CTA, 2009. Chemical and physical fronts in the Bohai, Yellow and East China seas. *Journal of Marine Systems* **78** (3), 394-410. https://doi.org/10.1016/j.jmarsys.2008.11.016.
12. He MX, Chen G, Sugimori Y, 1995. Investigation of mesoscale fronts, eddies and upwelling in the China Seas with satellite data. *The Global Atmosphere and Ocean System* **3** (4), 273-288.
13. He SY, Huang DJ, Zeng DY, 2016. Double SST fronts observed from MODIS data in the East China Sea off the Zhejiang–Fujian coast, China. *Journal of Marine Systems* **154**, 93-102. http://dx.doi.org/10.1016/j.jmarsys.2015.02.009.
14. Hickox R, Belkin I, Cornillon P, Shan Z, 2000. Climatology and seasonal variability of ocean fronts in the East China, Yellow and Bohai Seas from satellite SST data. *Geophysical Research Letters* **27** (18), 2945-2948. https://doi.org/10.1029/1999GL011223.
15. Hu MN, Zhao CF, 2008. Upwelling in Zhejiang coastal areas during summer detected by satellite observations. *Journal of Remote Sensing* **12** (2), 297-304. (In Chinese)
16. Hu ZF, Xie GH, Zhao J, Lei YP, Xie JC, Pang WH, 2022. Mapping diurnal variability of the wintertime Pearl River plume front from Himawari-8 geostationary satellite observations. *Water* **14** (1), Article 43. https://doi.org/10.3390/w14010043.
17. Huang DJ, Zhang T, Zhou F, 2010. Sea-surface temperature fronts in the Yellow and East China Seas from TRMM microwave imager data. *Deep Sea Research Part II* **57** (11-12), 1017-1024. https://doi.org/10.1016/j.dsr2.2010.02.003.
18. Lee MA, Chang Y, Shimada T, 2015. Seasonal evolution of fine-scale sea surface temperature fronts in the East China Sea. *Deep-Sea Research Part II* **119**, 20-29. https://doi.org/10.1016/j.dsr2.2014.03.021.
19. Li CY, Hu JY, Jan S, Wei ZX, Fang GH, Zheng QA, 2006. Winter-spring fronts in Taiwan Strait. *Journal of Geophysical Research: Oceans* **111** (11), Article C11S13. https://doi.org/10.1029/2005JC003203.
20. Liu DY, Wang Y, Wang YQ, Keesing JK, 2018. Ocean fronts construct spatial zonation in microfossil assemblages. *Global Ecology and Biogeography* **27** (10), 1225-1237. https://doi.org/10.1111/geb.12779.
21. Liu ZQ, Gan JP, Hu JY, Wu H, Cai ZY, Deng YF, 2021. Progress on circulation dynamics in the East China Sea and southern Yellow Sea: Origination, pathways, and destinations of shelf currents. *Progress in Oceanography* **193**, Article 102553. https://doi.org/10.1016/j.pocean.2021.102553.
22. Lou XL, Shi AQ, Xiao QM, Zhang HG, 2011. Satellite observation of the Zhejiang Coastal Upwelling in the East China Sea during 2007-2009. *Proceedings of SPIE*, Volume **8175**, Article 81751M. https://doi.org/10.1117/12.898140.

23. Minnett PJ, Alvera-Azcárate A, Chin TM, Corlett GK, Gentemann CL, Karagali I, Li X, Marsouin A, Marullo S, Maturi E, Santoleri R, Saux Picart S, Steele M, Vazquez-Cuervo J, 2019. Half a century of satellite remote sensing of sea-surface temperature. *Remote Sensing of Environment* **233**, Article 111366. https://doi.org/10.1016/j.rse.2019.111366.
24. Ning X, Liu Z, Cai Y, Fang M, Chai F, 1998. Physicobiological oceanographic remote sensing of the East China Sea: Satellite and in situ observations. *Journal of Geophysical Research***:** Oceans **103** (C10), 21623-21635. https://doi.org/10.1029/98JC01612.
25. Pan YQ, Xu DR, Xu JP, 1987. The structure of fronts and their causes in the coastal upwelling area off Zhejiang, China. *Acta Oceanologica Sinica* **6** (2), 177-189.
26. Park SH, Chu PC, 2006. Thermal and haline fronts in the Yellow/East China Seas: Surface and subsurface seasonality comparison. *Journal of Oceanography* **62** (5), 617-638. https://doi.org/10.1007/s10872-006-0081-3.
27. Pi QL, Hu JY, 2010. Analysis of sea surface temperature fronts in the Taiwan Strait and its adjacent area using an advanced edge detection method. *Science China Earth Sciences* **53** (7), 1008-1016. https://doi.org/10.1007/s11430-010-3060-x.
28. Ping B, Su FZ, Meng YS, Du YY, Fang SH, 2016. Application of a sea surface temperature front composite algorithm in the Bohai, Yellow, and East China Seas. *Chinese Journal of Oceanology and Limnology* **34** (3), 597-607. http://dx.doi.org/10.1007/s00343-015-4356-7.
29. Qi L, Hu CM, Liu JQ, Ma RH, Zhang YJ, Zhang S, 2022. *Noctiluca blooms* in the East China Sea bounded by ocean fronts. *Harmful Algae* **112**, Article 102172. https://doi.org/10.1016/j.hal.2022.102172.
30. Qiao FL, Yang YZ, Lü XG, Xia CS, Chen XY, Wang BD, Yuan YL, 2006. Coastal upwelling in the East China Sea in winter. *Journal of Geophysical Research: Oceans* **111** (C11), Article C11S06. https://doi.org/10.1029/2005JC003264.
31. Qiao LL, Liu SD, Xue WJ, Liu P, Hu RJ, Sun HF, Zhong Y, 2020. Spatiotemporal variations in suspended sediments over the inner shelf of the East China Sea with the effect of oceanic fronts. *Estuarine Coastal and Shelf Science* **234**, Article 106600. https://doi.org/10.1016/j.ecss.2020.106600.
32. Shimada T, Sakaida F, Kawamura H, Okumura T, 2005. Application of an edge detection method to satellite images for distinguishing sea surface temperature fronts near the Japanese coast. *Remote Sensing of Environment* **98** (1), 21-34. https://doi.org/10.1016/j.rse.2005.05.018.
33. Wang DX, Liu Y, Qi YQ, Shi P, 2001. Seasonal variability of thermal fronts in the Northern South China Sea from satellite data. *Geophysical Research Letters* **28** (20), 3963-3966. https://doi.org/10.1029/2001GL013306.
34. Wang YC, Chen WY, Chang Y, Lee MA, 2013. Ichthyoplankton community associated with oceanic fronts in early winter on the continental shelf of the southern East China Sea. *Journal of Marine Science and Technology* **21** (Suppl.), 65-76. https://doi.org/10.6119/JMST-013-1219-6.
35. Wang YC, Chan JW, Lan YC, Yang WC, Lee MA, 2018. Satellite observation of the winter variation of sea surface temperature fronts in relation to the spatial distribution of ichthyoplankton in the continental shelf of the southern East China Sea. *International Journal of Remote Sensing* **39** (13), 4550-4564. https://doi.org/10.1080/01431161.2017.1407053.
36. Wang YT, Yu Y, Zhang Y, Zhang HR, Chai F, 2020. Distribution and variability of sea surface temperature fronts in the South China Sea. *Estuarine, Coastal and Shelf Science* **240**, 106793. https://doi.org/10.1016/j.ecss.2020.106793.
37. Zhao LH, Yang DT, Zhong R, Yin XQ, 2022. Interannual, seasonal, and monthly variability of sea surface temperature fronts in offshore China from 1982–2021. *Remote Sensing* **14** (21), 5336.